International Journal of
Molecular Sciences

MDPI

Article

Enhanced Performance of WO_3/SnO_2 Nanocomposite Electrodes with Redox-Active Electrolytes for Supercapacitors

Tamiru Deressa Morka and Masaki Ujihara *

Graduate Institute of Applied Science and Technology, National Taiwan University of Science and Technology, 43 Keelung Road, Taipei 10607, Taiwan
* Correspondence: masaki.ujihara@mail.ntust.edu.tw

Abstract: For effective supercapacitors, we developed a process involving chemical bath deposition, followed by electrochemical deposition and calcination, to produce WO_3/SnO_2 nanocomposite electrodes. In aqueous solutions, the hexagonal WO_3 microspheres were first chemically deposited on a carbon cloth, and then tin oxides were uniformly electrodeposited. The synthesized WO_3/SnO_2 nanocomposite was characterized by XRD, XPS, SEM, and EDX techniques. Electrochemical properties of the WO_3/SnO_2 nanocomposite were analyzed by cyclic voltammetry, galvanostatic charge-discharge tests, and electrochemical impedance spectroscopy in an aqueous solution of Na_2SO_4 with/without the redox-active electrolyte $K_3Fe(CN)_6$. $K_3Fe(CN)_6$ exhibited a synergetic effect on the electrochemical performance of the WO_3/SnO_2 nanocomposite electrode, with a specific capacitance of 640 F/g at a scan rate of 5 mV/s, while that without $K_3Fe(CN)_6$ was 530 F/g. The WO_3/SnO_2 nanocomposite catalyzed the redox reactions of $[Fe(CN)_6]^3/[Fe(CN)_6]^{4-}$ ions, and the $[Fe(CN)_6]^{3-}/[Fe(CN)_6]^{4-}$ ions also promoted redox reactions of the WO_3/SnO_2 nanocomposite. A symmetrical configuration of the nanocomposite electrodes provided good cycling stability (coulombic efficiency of 99.6% over 2000 cycles) and satisfied both energy density (60 $Whkg^{-1}$) and power density (540 Wkg^{-1}) requirements. Thus, the WO_3/SnO_2 nanocomposite prepared by this simple process is a promising component for a hybrid pseudocapacitor system with a redox-flow battery mechanism.

Keywords: supercapacitor; nanocomposite; energy storage; redox-additive; tungsten oxide; tin oxide

check for updates

Citation: Morka, T.D.; Ujihara, M. Enhanced Performance of WO_3/SnO_2 Nanocomposite Electrodes with Redox-Active Electrolytes for Supercapacitors. *Int. J. Mol. Sci.* **2023**, *24*, 6045. https://doi.org/10.3390/ijms24076045

Academic Editor: Douglas B. Chrisey

Received: 9 February 2023
Revised: 1 March 2023
Accepted: 6 March 2023
Published: 23 March 2023

Copyright: © 2023 by the authors. Licensee MDPI, Basel, Switzerland. This article is an open access article distributed under the terms and conditions of the Creative Commons Attribution (CC BY) license (https://creativecommons.org/licenses/by/4.0/).

1. Introduction

Clean and renewable energy is the basic criterion for sustainable development of the global economy and human lives throughout the world [1]. The massive increase in fossil fuel usage has brought two significant problems: the first is rapidly reduced fossil fuel reserves, and the second is environmental degradation, such as air/water pollution and climate change. Considering these issues, the need for renewable energy and new technology for energy storage are currently the top concerns around the world. In response to rising ecological concern and modern civilization, new environmentally friendly and cost-effective energy storage devices with excellent performance are required for customer products, such as hybrid automobiles, electronic vehicles, mobile phones, and laptop computers [2,3]. Supercapacitors, batteries, and fuel cells are the most common electrochemical energy storage devices used for this purpose. Among them, supercapacitors are emphasized because of their excellent power densities, fast charge/discharge, long-term cycling life, cost-effectiveness, good reversibility, and wide working temperature range compared to those of batteries; however, in terms of commercial application, supercapacitors are behind batteries [4–6]. The fundamental issue of supercapacitors is their lower energy density, especially when compared to batteries.

To solve this problem of supercapacitors, three different energy storage mechanisms have been developed: electric double-layer capacitors (EDLCs), pseudocapacitor, and

battery-type capacitors [7]. Their energy storage mechanisms are explained as follows: the electric double-layer capacitor stores energy at the junction of the electrode and electrolyte by ion adsorption/desorption, the pseudocapacitor electrode stores energy on the surface of the electrode via Faradaic processes (using a fast and reversible redox process near the surface), and the battery-type capacitor has a specific potential window for the Faradaic processes used to enhance the capacitance [8]. During these electrochemical reactions, the amount of charge stored in the electrode is proportional to the total available surface of the active materials in the electrode. Therefore, porous materials with large specific surface areas are preferable for supercapacitors [1].

As active materials for pseudocapacitors, transition metal oxides (TMOs) and conducting polymers are widely used [9]. Transition metal oxides are known for high specific capacitance without sacrificing power density [10]. Among TMOs, RuO_2, Co_3O_4, ZnO, MoO_3, Fe_2O_3 MnO_2, NiO, SnO_2, WO_3, and others have been investigated as active materials due to their appealing characteristics, such as high theoretical capacitance and low environmental impact [2,8,11–13]. Furthermore, composite TMOs have been designed for a pseudocapacitor with expectations of synergistic effects [6,7]. The TMOs in the composite electrode can produce unique structures with large surface areas, and the mixed valence metals can provide an extra valance state for the electrochemical process, which results in improved performance of the supercapacitor [3,5].

Recently, tungsten trioxide (WO_3) has been considered a promising candidate for pseudocapacitors due to its numerous intrinsic features, such as high theoretical capacitance, high corrosion resistance, good chemical stability, low cost, and environmental friendliness [14], and a variety of composites with other TMOs, such as MnO_2-WO_3 [15], Ni-WO_3 [16], Co-WO_3 [17], TiO_2/WO_3 [18], WO_3/Se [2], and V_2O_5/WO_3 [19], have been examined. Moreover, SnO_2 has attracted much attention as an electrode for energy storage or conversion due to its low cost, nontoxicity, high electrochemical activity, and chemical stability [20]. For successful insertion of SnO_2 into WO_3, excellent electrochemical supercapacitor performance is required [21,22]. Hence, motivated by the above considerations, we investigated the WO_3/SnO_2 nanocomposite as an active electrode material for supercapacitors.

Another approach to enhancing the capacity of the supercapacitor is to use a redox-active electrolyte. The effects of additive electrolytes, such as $K_3Fe(CN)_6$ [23,24], KI [25], and p-aminophenol [26], have been reported for aqueous systems. The basic role of these additives is to improve charge transport in the electrolyte solution, adjust the chemical state of the working electrode surface, and enhance Faradaic reactions. Synergistic effects in electrochemical processes, both in the active materials and electrolytes, can also be expected to enhance the efficiencies of redox reactions and improve the performance of supercapacitors [23]. The electrolyte additive potassium ferricyanide, $K_3Fe(CN)_6$, enables the electrode of the supercapacitor to achieve fast charging, slow discharge, and good cycling stability [27]. In this work, we investigated the preparation of a WO_3/SnO_2 nanocomposite through chemical bath deposition (CBD) and electrodeposition on a carbon cloth substrate, and analyzed its supercapacitor performance by using $K_3Fe(CN)_6$ added into a 1 M Na_2SO_4 aqueous electrolyte [28]. To the best of our knowledge, this is the first trial to synthesize a WO_3/SnO_2 nanocomposite and to determine its electrochemical supercapacitance performance with the redox-active electrolyte K_3Fe $(CN)_6$ with Na_2SO_4, and the system demonstrated a specific capacitance of 640 F/g. A symmetric supercapacitor using a WO_3/SnO_2 nanocomposite and an additive electrolyte was further assembled to demonstrate the potential of this system for efficient energy storage.

The reaction mechanisms for formation of WO_3 were as follows (Equations (1) and (2)) [1,29]:

$$Na_2WO_4 + 2HCl + nH_2O \rightarrow H_2WO_4{\cdot}nH_2O + 2HO_4{\cdot}nH_2O \quad (1)$$

$$H_2WO_4{\cdot}nH_2O \rightarrow WO_3 + (n+1)H_2O \quad (2)$$

Crystals of tungsten oxide (WO_3) are polymorphic and often adopt a hexagonal system [1,15]. Various synthetic aspects, such as the reaction temperature, process duration, precursor type, and chemical agent (e.g., $(NH_4)_2SO_4$), can influence the structure and morphology. In comparison to other structures, this structure provides large tunnels for ion penetration, which improves the electrochemical performance [13]. Thus, WO_3 is usually synthesized as a hexagonal system using reagents containing sulfate ions; in particular, ammonium sulfate is preferred. The NH_4^+ and SO_4^{2-} ions act as stabilizing and capping agents, respectively, during the process. The radius of the NH_4 ion is larger than those of alkali metal ions, and these differences in size influence the penetration of numerous ions, which implies that many SO_4^{2-} ions can readily be adsorbed on the surface parallel to the WO_3 axis [13,30]. The morphology and crystal structure of WO_3 are also affected by the annealing temperature. The orthorhombic phase changes into an anhydrous hexagonal phase at 400 °C and turns into stable monoclinic WO_3 with aggregation above 500 °C [31]. Therefore, annealing in this work was done at 400 °C for 2 h.

2. Results

2.1. Characterization of WO_3, SnO_2, and WO_3/SnO_2 Nanocomposite Thin Films

The structural characteristics and crystal phases of the WO_3, SnO_2, and WO_3/SnO_2 nanocomposites were analyzed by XRD (Figure 1). The XRD peaks for WO_3 were assigned to the hexagonal system, except for the one marked with an asterisk; this came from the carbon cloth substrate (Figure 1a). The diffraction peaks at 2θ = 14.25°, 23.28°, 28.2°, 34.8°, 37.28°, 44.30°, 50.28°, 52.40°, and 56.03° were assigned to the (100), (110), (200), (112), (202), (212), (004), (220), and (204) planes, respectively (JCPDS 85-2459). The sharp and intense peaks suggested the highly crystalline nature of the WO_3.

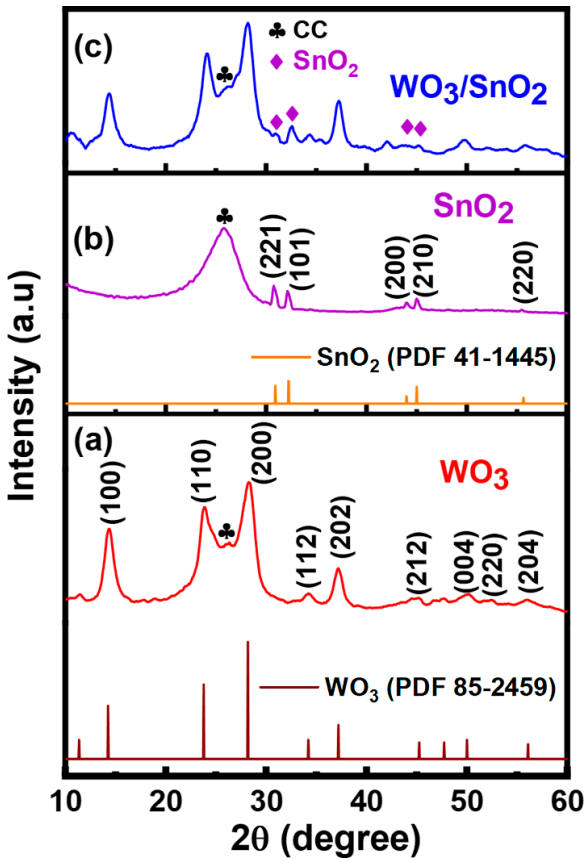


Figure 1. XRD patterns for (**a**) WO_3, (**b**) SnO_2, and (**c**) WO_3/SnO_2 nanocomposites. The clubs (♣) and diamonds (♦) represent peaks of CC and SnO_2, respectively.

The XRD pattern for the synthesized SnO_2 showed sharp diffraction peaks at 30.7°, 32.1°, 43.9°, 45.1°, and 55.5°, which corresponded to the (221), (101), (111), (210), and (220) planes of the tetragonal phase (JCPDS 41-1445), respectively, except for the one marked with an asterisk, which came from the carbon cloth substrate (Figure 1b) [32]. Figure 1c shows the diffraction peaks for the WO_3/SnO_2 nanocomposite at 2θ = 14.25°, 23.28°, 28.20°, 30.71°, 32.10°, 34.80°, 37.28°, 43.20°, 44.30°, 45.10°, 50.28°, 52.40°, 55.20°, and 56.03°, which were assigned to the (100), (110), (200), (112), (202), (212), (004), (220), and (204) planes of WO_3 and (221), (101), (111), (210), and (220) planes of SnO_2, respectively. The diffraction peaks, denoted with diamond symbols, were indexed to the tetragonal structure of SnO_2 [33]; similarly, the other peaks were associated with the hexagonal crystal phase of WO_3 [1]. Therefore, this diffraction pattern was composed of characteristic peaks for both WO_3 and SnO_2, as observed in (Figure 1a,b), which confirmed successful preparation of the WO_3/SnO_2 nanocomposite. No new significant peak was observed, and thus, the WO_3 and SnO_2 components were separately crystallized in the nanocomposite. The presence of sharp diffraction peaks suggested the highly crystalline nature of the materials deposited on the carbon cloth substrate. The average sizes of the WO_3 and SnO_2 crystallites in the WO_3/SnO_2 nanocomposite were determined by the Scherrer equation, as shown below in (Equation (3)) [6,34–36]:

$$D = K/\beta\cos\theta \quad (3)$$

where D is the crystallite size (nm), β is the full width half maximum (FWHM, radians) of the peak corresponding to the plane, K = 0.9 (Sherrer constant), λ = 0.15406 nm (wavelength of the X-ray source), and θ is obtained from the 2θ value corresponding to the diffraction peak [35]. These findings showed that the average crystallite sizes for the WO_3 synthesized in the nanocomposite were 7.5 nm, with diffraction peaks of 2θ = 23.28° and 28.2° for the corresponding (110) and (200) planes, respectively. The average crystallite size of the SnO_2 synthesized in the nanocomposite was estimated to be 3.9 nm, with diffraction peaks at 2θ = 32.10°, with a corresponding (101) plane [37,38].

The chemical compositions and surfaces of the WO_3, SnO_2, and WO_3/SnO_2 nanocomposites were further investigated using XPS (Figure 2 and Table 1). The survey spectrum for the WO_3/SnO_2 nanocomposite showed the coexistence of W, Sn, O, and C elements, and no other impurity peak was significantly detected (Figure 2a).

The high-resolution W 4f spectrum for WO_3 was deconvoluted into two peaks (Figure 2b). The peaks at 36.08 eV and 38.21 eV were assigned to W $4f_{7/2}$ and W $4f_{5/2}$ binding energies, respectively, corresponding to the W^{6+} oxidation state. The separation between the W $4f_{7/2}$ and W $4f_{5/2}$ peaks was 2.13 eV, which was in good agreement with an earlier report [1]. Figure 2c shows the O 1s peak at 531.1 eV, which was assigned to the lattice oxygens of W–O bonds in WO_3. The peak at 532.01 eV was due to an oxygen deficiency, the peak at 532.7 eV was assigned to chemisorbed oxygen, and the peak at 533.6 eV was attributed to water and hydroxide. Figure 3d shows the high-resolution Sn 3d spectrum of pure SnO_2, which was deconvoluted into two peaks with binding energies of 487.6 eV and 496.05 eV. These peaks were assigned to the Sn $3d_{5/2}$ and Sn $3d_{3/2}$ binding energies, respectively, for the oxidation state Sn^{4+}. The splitting between the Sn $3d_{5/2}$ and Sn $3d_{3/2}$ peaks was 8.45 eV, which was in good agreement with a previous study [4]. As displayed in (Figure 2e), the O 1s spectrum was deconvoluted into three peaks at 531.5 eV for lattice SnO_2, chemisorbed oxygen at 532.7 eV, and water and hydroxide at 534.3 eV. In the WO_3/SnO_2 nanocomposite, the W 4f spectrum showed two peaks at 35.74 eV and 38.08 eV, which corresponded to W $4f_{7/2}$ and W $4f_{5/2}$ binding energies, respectively, and an oxidation state of W^{+6} (Figure 2f). The spin–orbit separation of W $4f_{7/2}$ and W $4f_{5/2}$ was 2.24 eV, which agreed with previous reports [39]. The difference in the W 4f doublet separation for the WO_3 and WO_3/SnO_2 nanocomposites (2.13 eV and 2.24 eV, respectively) was also reported in an earlier study [2]: the W $4f_{7/2}$ peak was shifted by −0.24 eV, and the W $4f_{5/2}$ peak was shifted by −0.13 eV, which suggested an interaction between WO_3 and SnO_2 (Table 1). Moreover, the Sn 3d spectrum of the WO_3/SnO_2 composite had two peaks at 487.69 eV and 496.12 eV, which corresponded to the characteristic Sn $3d_{5/2}$ and Sn $3d_{3/2}$

binding energies, respectively. The spin–orbit separation between the Sn $3d_{5/2}$ and Sn $3d_{3/2}$ peaks was 8.43 eV (Figure 2g), which agreed with earlier reports [40]. Comparing pure SnO_2 and WO_3/SnO_2, the Sn $3d_{5/2}$ and Sn $3d_{3/2}$ peaks were slightly shifted by 0.02 eV, which could have been due to an interaction between WO_3 and SnO_2. The O 1s spectrum was deconvoluted into four peaks (Figure 2h) at 531.09 eV, 531.76 eV, 532.8 eV, and 534.3 eV. The main peak at 531.76 eV was attributed to lattice oxygens in the metal oxides WO_3 and SnO_2 [33,37,40], the peak at 531.09 eV was assigned to oxygen defects or vacancies, the peak at 532.8 eV was related to chemisorbed oxygen species [41], and the peak at 534.3 eV was attributed to water and hydroxides on the surface of the WO_3/SnO_2 nanocomposite, as reported previously [6,32,40]. The binding energies of the lattice oxygens and oxygen vacancies in the WO_3/SnO_2 nanocomposite were shifted from those of the single components by −0.34 eV and 0.25 eV, respectively, which suggested an interaction between WO_3 and SnO_2 in the nanocomposite. The binding energy for absorbed water/hydroxides in the nanocomposite was similar to that of SnO_2, which suggested that the surface of the nanocomposite was covered by SnO_2.

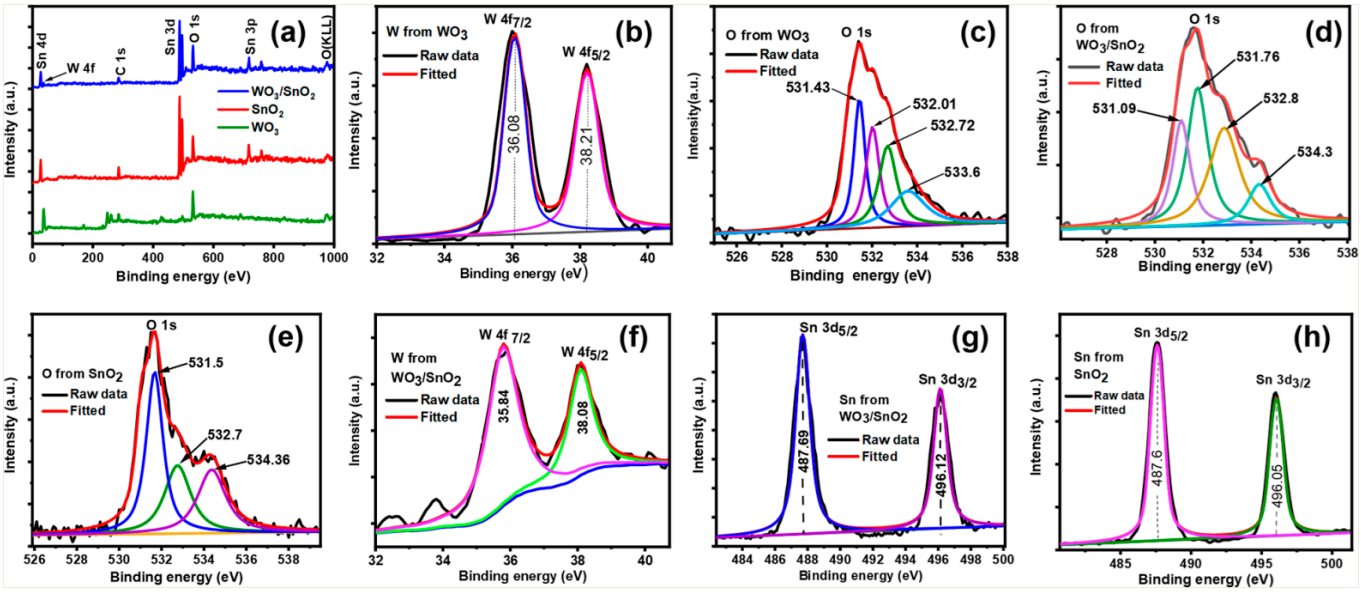


Figure 2. XPS data for WO_3, SnO_2, and the WO_3/SnO_2 nanocomposite: (**a**) survey spectrum of the WO_3/SnO_2 nanocomposite, high-resolution (**b**) W 4f spectrum of WO_3, (**c**) O 1s spectrum of WO_3, (**d**) Sn 3d spectrum of SnO_2, (**e**) O 1s spectrum of SnO_2, (**f**) W 4f spectrum of WO_3/SnO_2, (**g**) Sn 3d spectrum of WO_3/SnO_2, and (**h**) O 1s spectrum of the WO_3/SnO_2 nanocomposite.

Table 1. Binding energies (eV) for W, Sn, and O in WO_3, SnO_2, and WO_3/SnO_2 nanocomposites determined by deconvolution of XPS peaks.

		W $4f_{7/2}$	**W $4f_{5/2}$**	**Doublet Separation**
WO_3		36.08	38.21	2.13
WO_3/SnO_2		35.84	38.08	2.24
		Sn $3d_{5/2}$	Sn $3d_{3/2}$	
SnO_2		487.60	496.05	8.45
WO_3/SnO_2		487.69	496.12	8.43
	O in Lattice Metal Oxide	O Deficiency (Defects)	Chemisorbed O	O in Water, Hydroxide (OH^-/H_2O)
WO_3	531.43	532.01	532.72	533.60
SnO_2	531.50	-	532.70	534.38
WO_3/SnO_2	531.09	531.76	532.80	534.30

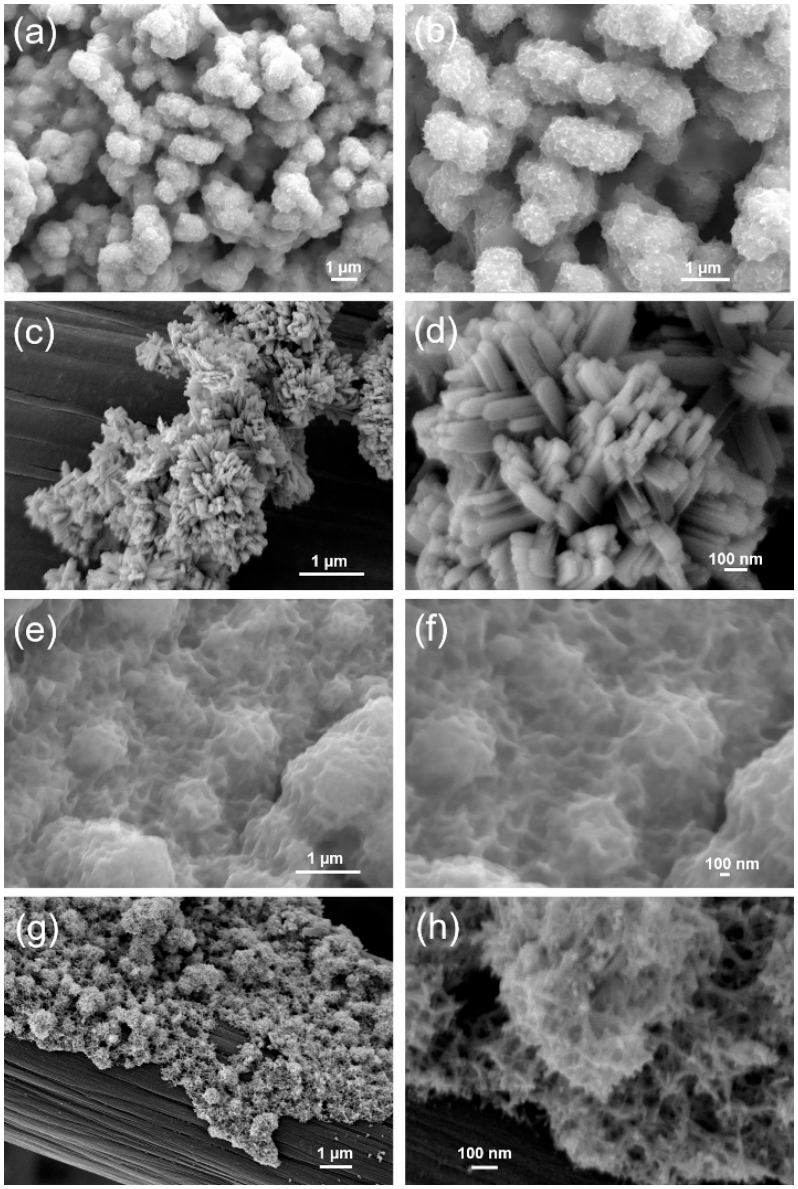


Figure 3. FE-SEM images of (**a**,**b**) WO_3 grown on a carbon cloth, (**c**,**d**) SnO_2 grown on a carbon cloth, (**e**,**f**) WO_3/SnO_2 nanocomposite, and (**g**,**h**) cross-sectional image of WO_3/SnO_2 nanocomposite at low and high magnification, respectively.

The morphologies of the materials were observed by SEM. WO_3 was composed of aggregated monodisperse microspheres (diameter: ~1 μm) with rough surfaces (Figure 3a,b). The spaces between these microspheres would allow electrolyte ions to diffuse into the porous nanostructure [15,42]. The roughness of the microsphere surface increased the number of active sites available for electrochemical reactions. Moreover, the SnO_2 exhibited nanorod structures with ~60 nm widths and ~200 nm lengths (Figure 3c,d). The applied potential and the deposition time are crucial for successful formation of SnO_2 nanorods [43,44]. In this work, SnO_2 nanorods were synthesized from $SnCl_2$ on a cathode (−0.9 V vs. Ag/AgCl), and the formation of SnO_2 crystals can be attributed to electrochemical deposition of $Sn(OH)_2$, followed by air oxidation during calcination, as shown below (Equations (4)–(7)) [45]:

$$SnCl_2 + 2OH \rightarrow Sn(OH)_2 + 2Cl^- \quad (4)$$

$$Sn(OH)_2 \rightarrow SnO + H_2O \quad (5)$$

$$SnO + 1/2\ O_2 \rightarrow SnO_2 \quad (6)$$

$$Sn(OH)_2 + 1/2\ O_2 + H_2O \rightarrow Sn(OH)_4 \rightarrow SnO_2 + 2H_2O \quad (7)$$

The SEM images in (Figure 3e,f) indicate the surface morphology of the WO_3/SnO_2 nanocomposite. Thin and wrinkled films were uniformly formed on the substrate. These films seemed to cover microspheres, which could be the WO_3 first deposited on the carbon cloth substrate. This morphology suggested that SnO_2 could not form coarse nanorods on the rough surfaces of WO_3, so smaller SnO_2 crystals formed a network on the surface [46]. In the cross-sectional views (Figure 3g,h), the surface of WO_3 was covered by nanorods of SnO_2 [47]. These small crystals and the fine nanorods provide a large surface area, which could enhance the electrochemical performance of this nanocomposite [32].

The elemental compositions of the synthesized materials were measured with EDS (Figure 4). In the pure WO_3 microspheres, the atomic ratio of W to O was 1:3.09, which agreed with the theoretical ratio of 1:3. In the SnO_2 nanorods, the atomic ratio of Sn to O was 1:1.58, which was lower than the theoretical ratio of 1:2, suggesting that unreacted Sn^{2+} provided defects or oxygen vacancies in the crystal lattice. The WO_3/SnO_2 nanocomposite consisted of W, Sn, and O, with atomic percentages of W (18.45%), Sn (6.31%), and O (75.24%). The Sn content was significantly lower than the W content, which was supported by the SEM observation (Figure 3e,f). The elemental maps (Figure 4d–g) showed similar patterns for the components, which suggests homogeneous coverage of SnO_2 on the WO_3 microspheres.

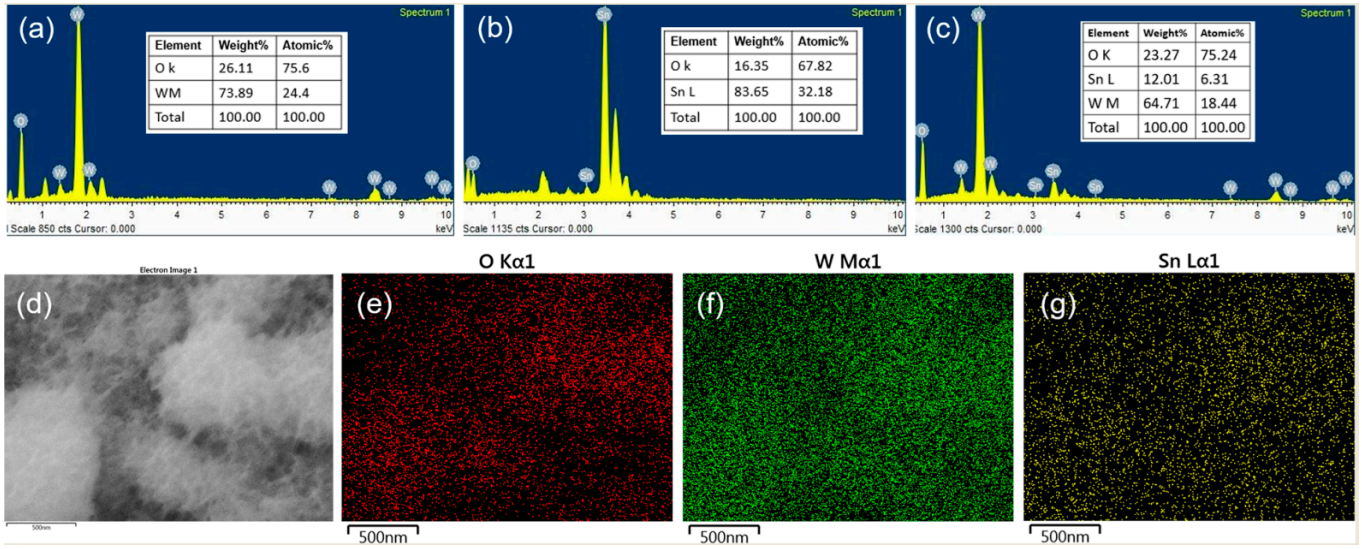


Figure 4. EDS spectra of synthesized (**a**) WO_3 microspheres, (**b**) SnO_2 nanorods, and (**c**) WO_3/SnO_2 nano-composites; (**d**) SEM image and elemental maps of WO_3/SnO_2 nanocomposites for (**e**) O, (**f**) W, and (**g**) Sn.

2.2. Electrochemical Measurements

2.2.1. Electrochemical Measurements without a Redox-Active Electrolyte

The electrochemical behaviors of the synthesized materials were analyzed with CV and GCD measurements using the non-redox electrolyte Na_2SO_4 (Figures 5 and 6).

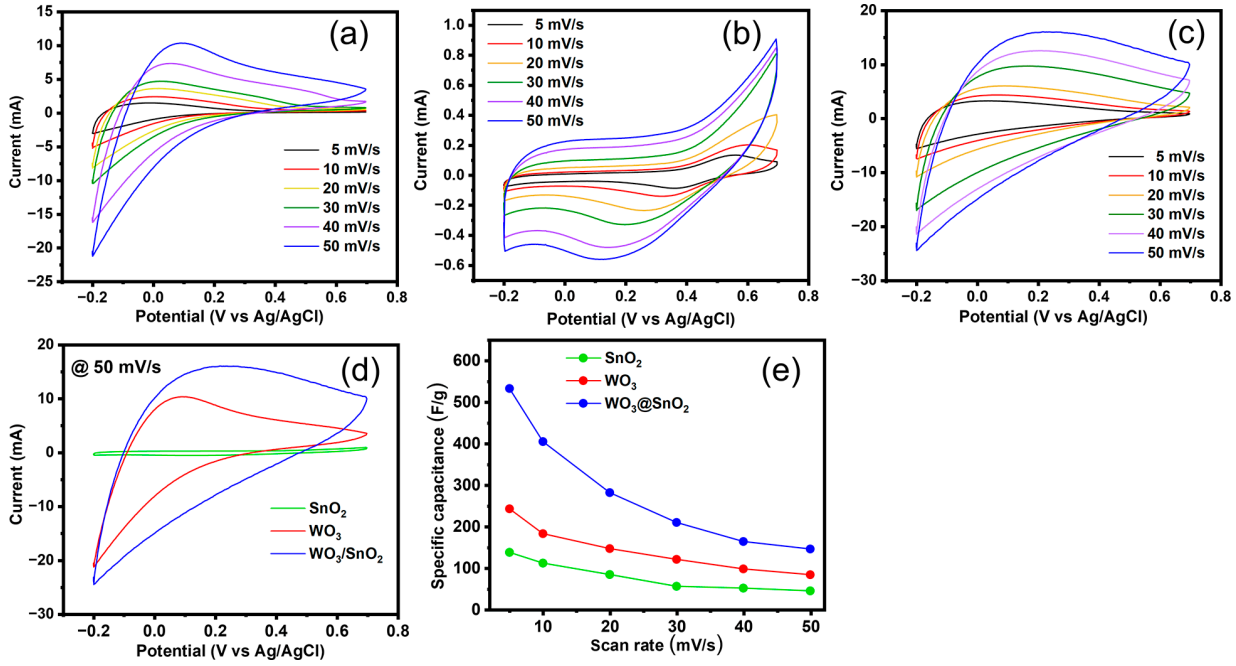


Figure 5. CV curves for (**a**) WO_3, (**b**) SnO_2, and (**c**) WO_3/SnO_2 nanocomposite electrodes at various scan rates from 5 mV/s to 50 mV/s with 1 M Na_2SO_4 electrolyte; (**d**) comparison of CV curves for WO_3, SnO_2, and WO_3/SnO_2 at 50 mV/s; (**e**) specific capacitance vs. scan rate for WO_3, SnO_2, and WO_3/SnO_2 from CV curves.

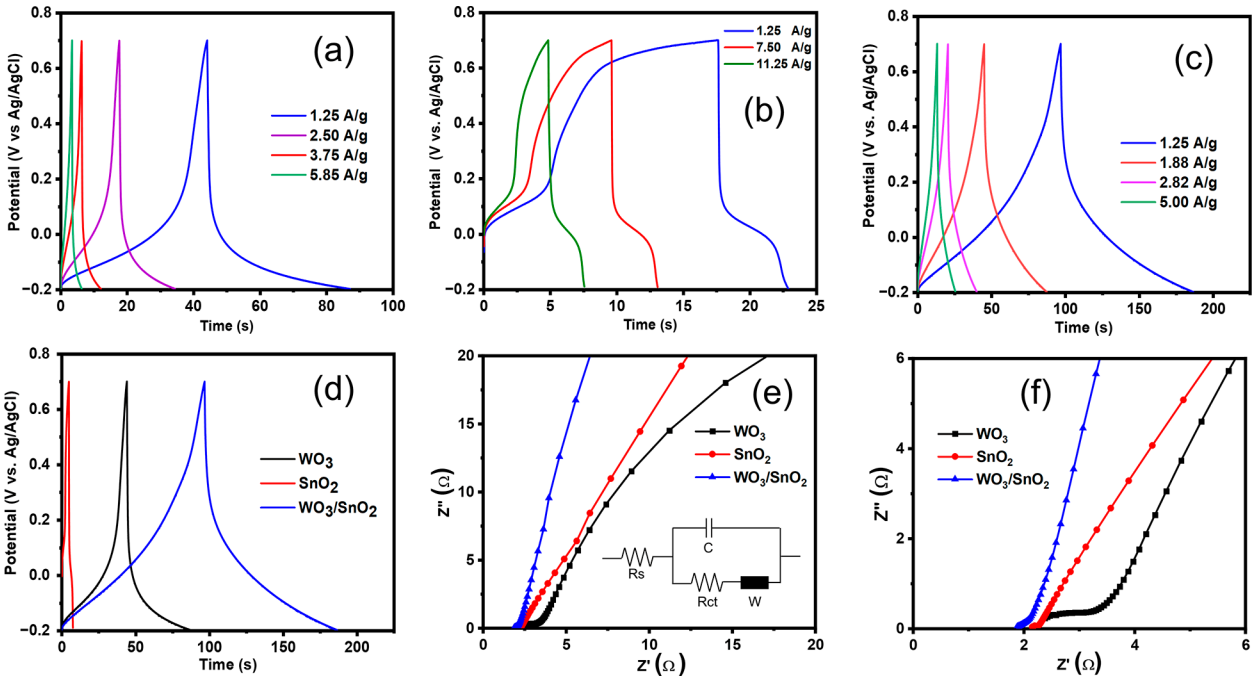


Figure 6. GCD curves determined for electrodes with 1 M Na_2SO_4 electrolyte and at different current densities: (**a**) WO_3, (**b**) SnO_2, and (**c**) WO_3/SnO_2; (**d**) comparison of GCD curves for WO_3, SnO_2, and WO_3/SnO_2 with the same current density of 1.25 A/g; (**e**) EIS for WO_3, SnO_2, and WO_3/SnO_2 nanocomposite electrodes; and (**f**) magnified EIS for the inset in (**e**), and the inset in (**e**) is the model circuit used for the analysis.

Figure 5a shows the CV curves for WO_3 in the potential window −0.2 to 0.7 V vs. Ag/AgCl with various scan rates of 5–50 mV/s. These CV curves demonstrated nonrectan-

gular shapes and medium oxidation peaks at approximately 0.1 V, which indicated a typical combination of pseudocapacitive behavior and electrical double-layer capacitance [48,49]. The oxidation peak clearly increased as the scan rate was increased, indicating the high reactivity of the WO_3 electrode [50,51]. The specific capacitance was determined from the CV curves by using (Equation (8)) [9,52–54]:

$$\mathrm{Ccv}(\mathrm{Fg}^{-1}) = \frac{1}{mv(Vf - Vi)} \int_{V_i}^{V_f} idV \tag{8}$$

where C_{cv} is the gravimetric specific capacitance (F/g) calculated from the measurement, i is the voltammetric current, m is the mass of the active material (mg), ν is the scan rate (mV/s), V_f and V_i are the bounds of the potential window. The C_{cv} of the WO_3 electrode was 240, 180, 150, 120, 98, and 84 F/g at scan rates of 5, 10, 20, 30, 40, and 50 mV^{-1}, respectively.

Under the same conditions, the CV curves for SnO_2 displayed quasi-rectangular shapes, with redox peaks at 0.54–0.69 V (oxidative) and 0.12–0.37 V (reductive), which indicated the more pseudocapacitive nature of the SnO_2 electrode (Figure 5b). As the scan rate was increased, the CV curves for SnO_2 exhibited more rectangular shapes, and the difference between the redox peaks increased, which suggested relatively slow redox reactions occurring on the surfaces of the SnO_2 nanorods. The specific capacitance values for the SnO_2 electrodes were calculated from the CV curves and were 140, 120, 90, 60, 50, and 45 F/g at scan rates of 5, 10, 20, 30, 40, and 50 mV/s, respectively, as shown in (Figure 5e). The CV curves for the WO_3/SnO_2 nanocomposite showed no significant redox peak (Figure 5c), which suggested the complementary work of the two components and a synergistic effect arising from interactions between WO_3 and SnO_2 (see Figure 2 and Table 1). This WO_3/SnO_2 nanocomposite electrode generated greater areas under the CV curves, which indicated a higher specific capacitance than the single-component electrodes (WO_3 and SnO_2) (Figure 5e). The specific capacitances of the WO_3/SnO_2 nanocomposite were calculated as 530, 410, 280, 210, 160, and 150 Fg^{-1} at scan rates of 5, 10, 20, 30, 40, and 50 mV s^{-1}, respectively. Comparing the CV curves and the specific capacitances of the three electrodes, the WO_3/SnO_2 nanocomposite electrode had a higher specific capacitance, especially at low scan rates (Figure 5d,e). This enhanced performance for the nanocomposite electrode could be explained by activation of the SnO_2 via the synergistic effect and the smaller crystals of SnO_2 formed on WO_3 (Figure 4). The small SnO_2 crystals could have enhanced the surface area of the electrode and shortened the electron pathway from the surface of SnO_2 to WO_3 [55].

Figure 6a illustrates the GCD curves of the WO_3 electrode in the potential window—0.2 to 0.7 V vs. Ag/AgCl at various current densities. The nonlinear nature of the charge/discharge processes confirmed the pseudocapacitive nature and the high activity at low potential (<0.1 V). The specific capacitance was calculated from the GCD curves and Equation (9) [9,53,54]:

$$\mathrm{C_G}(\mathrm{Fg}^{-1}) = \mathrm{Ig} \int dt/m\Delta V(t) \tag{9}$$

where C_G is the gravimetric capacitance (F/g) from the GCD measurement, I_g is the given current, dt is the discharging time (s), and $\Delta V(t)$ is the potential window as a function of t. The C_G of WO_3 electrode was calculated to be 120 Fg^{-1} at a current density of 1.25 Ag^{-1}. The SnO_2 electrode exhibited two steps in the charge process and one step in the discharge process (Figure 6b). At 1.25 Ag^{-1}, the specific capacitance of the SnO_2 electrode was 54 Fg^{-1}. Figure 6c shows the GCD curves for the WO_3/SnO_2 nanocomposite electrode at different current densities. The shapes of the GCD curves were more triangular, which indicated that the nanocomposite electrode exhibited better pseudocapacitive nature than the others, as was also suggested by the CV measurements (Figure 6). The specific capacitance of the WO_3/SnO_2 nanocomposite was determined to be 180, 120, 80, and 68 Fg^{-1} at the various current densities 1.25, 1.88, 2.82, and 5.00 Ag^{-1}, respectively. Figure 6d provides a comparison of the GCD curves for the SnO_2, WO_3, and WO_3/SnO_2 electrodes at the same current density of 1.25 Ag^{-1}. Figure 6e shows the EIS results for the WO_3, SnO_2, and

WO_3/SnO_2 nanocomposite electrodes, and the magnified EIS data for the electrode are shown in (Figure 6f). The charge transfer resistance values (Rct) calculated for the WO_3, SnO_2, and WO_3/SnO_2 nanocomposite electrodes were 2.12 Ω, 1.94 Ω, and 1.72 Ω, respectively. The lower Rct of the WO_3/SnO_2 nanocomposite electrode indicated rapid charge transfer in the nanocomposite. The resistance of the electrode–electrolyte interference (Rs), which corresponds to the *x*-axis intercept in the high-frequency region, was calculated to be 2.37 Ω, 2.32 Ω, and 1.87 Ω for the WO_3, SnO_2, and WO_3/SnO_2 nanocomposite electrodes, respectively. The low Rs suggested that the WO_3/SnO_2 nanocomposite contacted the electrolytes with large surface areas because of its small grain sizes (Figure 4).

2.2.2. Effects of Redox-Active Electrolyte

Electrochemical analyses of the WO_3, SnO_2, and WO_3/SnO_2 electrodes were performed in the presence of the redox additive 0.2 M $K_3Fe(CN)_6$ in the 1 M Na_2SO_4 aqueous electrolyte. First, CV measurements were conducted with the carbon cloth, WO_3, SnO_2, and WO_3/SnO_2 nanocomposite electrodes (Figure 7a).

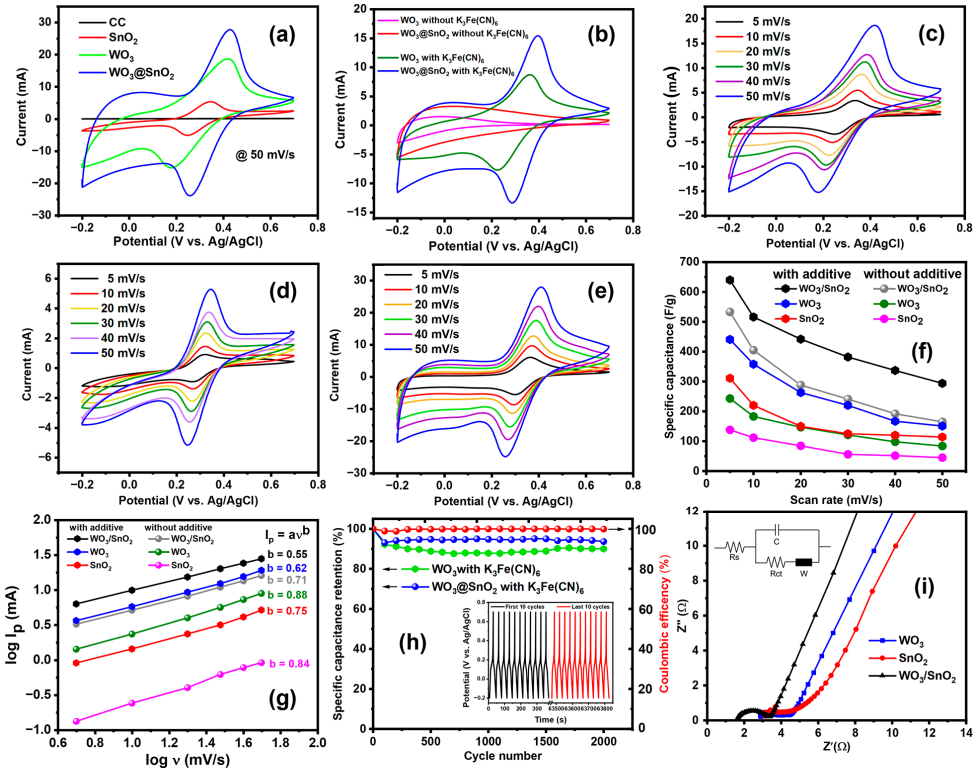


Figure 7. CV curves for (**a**) various electrodes at scan rate of 50 mV/s with $K_3Fe(CN)_6$ and (**b**) WO_3 and the WO_3/SnO_2 nanocomposite electrodes with/without $K_3Fe(CN)_6$ at scan rate of 30 mV/s; CV curves of (**c**) WO_3 electrode, (**d**) SnO_2 electrode, and (**e**) WO_3/SnO_2 nanocomposite electrode with $K_3Fe(CN)_6$ at various scan rates; (**f**) specific capacitance of various electrodes with/without $K_3Fe(CN)_6$ at various scan rates; (**g**) double logarithmic plots of scan rate vs. peak current for WO_3, SnO_2, and the WO_3/SnO_2 nanocomposite; (**h**) cycling stability and coulombic efficiency versus cycle number for the WO_3/SnO_2 nanocomposite electrode with $K_3Fe(CN)_6$; (**i**) EIS analyses of WO_3, SnO_2, and WO_3/SnO_2 nanocomposite electrodes with $K_3Fe(CN)_6$ over the frequency range 100 kHz to 100 mHz.

While the carbon cloth was almost inactive, the CV curves for the metal oxide electrodes exhibited quasi-rectangular shapes, with a pair of redox peaks from $[Fe(CN)_6]^{3-}/[Fe(CN)_6]^{4-}$ at 0.35–0.43 V and 0.18–0.26 V. The WO_3/SnO_2 nanocomposite electrode had the largest area at a scan rate of 50 mV/s, which indicated the highest specific capacitance. The WO_3/SnO_2 nanocomposite electrode also resulted in higher intensities of redox peaks than

the other electrodes, which indicated that this electrode exhibited the highest activity for the redox reactions of $[Fe(CN)_6]^{3-}/[Fe(CN)_6]^{4-}$. Moreover, considering the high peak intensities, the difference between the oxidation and reduction potentials was smaller than those of the other electrodes. The reduction peak for $[Fe(CN)_6]^{3-}$ with the WO_3/SnO_2 nanocomposite electrode was at the highest potential among the electrodes, while the oxidation potential for $[Fe(CN)_6]^{4-}$ with the WO_3/SnO_2 nanocomposite electrode was higher than the others. These behaviors suggested that the WO_3/SnO_2 nanocomposite catalyzed the redox reactions of $[Fe(CN)_6]^{3-}/[Fe(CN)_6]^{4-}$, which is preferable for energy storage because of the low overpotential. The catalytic activity of the WO_3/SnO_2 nanocomposite could be due to interactions between WO_3 and SnO_2, as suggested by the XPS measurements (Figure 2 and Table 1). Therefore, the CV curves generated with two sets of conditions were compared, i.e., with $K_3Fe(CN)_6$ and without $K_3Fe(CN)_6$ (Figure 7b). With $K_3Fe(CN)_6$, the areas of the CV curves were larger, which indicated that the redox additive increased the charge storage capacity. Using the CV curves generated at different scan rates (Figure 7c–e), the specific capacitance of the electrode in the redox-active electrolyte was calculated. At scan rates of 5, 10, 20, 30, 40, and 50 mV/s, the respective specific capacitance values were 440, 360, 280, 240, 190, and 150 F/g for the WO_3 electrode; 310, 220, 150, 130, 120, and 110 F/g for the SnO_2 electrode; and 640, 520, 340, 330, 310, and 290 F/g for the WO_3/SnO_2 nanocomposite electrode. Moreover, the addition of $K_3Fe(CN)_6$ resulted in more pseudocapacitive (more rectangular CV curves) for the WO_3 and WO_3/SnO_2 nanocomposite electrodes. In details, weak and broad reduction bands newly appeared at −0.1–0.0 V for the WO_3 electrode and 0.0–0.1 V for the WO_3/SnO_2 electrode in the presence of $K_3Fe(CN)_6$ (Figure 7b,c,e). The pseudocapacitive behavior suggested that $K_3Fe(CN)_6$ provided the additional redox reactions of the $[Fe(CN)_6]^{3-}/[Fe(CN)_6]^{4-}$ couple to increase the specific capacitance of these electrodes [56,57], and also promoted the redox reactions of the WO_3 component. That is, these metal oxides (WO_3 and WO_3/SnO_2 nanocomposites) transferred electrons to the $[Fe(CN)_6]^{3-}/[Fe(CN)_6]^{4-}$ pair in the electrolyte solution via their own redox reactions. The plots of the specific capacitance for various electrodes against the different scan rates showed that only the WO_3/SnO_2 nanocomposite electrode exhibited a larger enhancement of the specific capacitance by $K_3Fe(CN)_6$ at the high scan rate versus the low scan rate (Figure 7f). This enhancement at the high scan rate was due to the catalytic activity of the WO_3/SnO_2 nanocomposite in facilitating the redox reactions of $[Fe(CN)_6]^{3-}/[Fe(CN)_6]^{4-}$, as mentioned above.

The kinetics of the energy storage process were analyzed from the perspectives of peak current and scan rate (Figure 7g). In general, the relationship between the peak current and the scan rate can be described as in (Equation (10)) [58,59]:

$$I_p = a\nu^b \quad (10)$$

where I_p is the peak oxidation current (mA), ν is the scan rate (mV/s), and both a and b are adjustable parameters. The b value is obtained from the slope of a plot of log I_p versus log ν. When the charge storage process is a surface-controlled capacitive process (ion adsorption/desorption), the value of b is 1. On the other hand, if diffusion is the rate-controlling process, b is 0.5 [60]. With and without the $K_3Fe(CN)_6$ electrolyte, the b values of the WO_3/SnO_2 nanocomposite electrode were 0.55 and 0.71, respectively. These b values suggested that addition of the $K_3Fe(CN)_6$ electrolyte favored diffusion control of the energy storage process because the approach of the redox-active species enabled charge transfer at the electrode surface. Moreover, the b values for the WO_3 and SnO_2 electrodes were 0.62 and 0.75, respectively. These b values were higher than that of the WO_3/SnO_2 nanocomposite electrode, which indicated that these single-component electrodes were less affected by diffusion of the redox-active species.

The GCD measurements made in the presence of the $K_3Fe(CN)_6$ electrolyte were not adequate to calculate the specific capacitance values of the synthesized electrodes because the discharge process took longer than the charge time (see Figure S1 in Supporting Information). This extension of the discharge process could be due to reduction of $[Fe(CN)_6]^{3-}$

to $[Fe(CN)_6]^{4-}$, which could be used for the redox-flow battery system. Therefore, GCD measurements were conducted for stability testing (Figure 7h). The coulombic efficiency of the electrode was calculated with Equation (11):

$$\eta = t_d / t_c \times 100 \quad (11)$$

where η is the coulombic efficiency, t_d is the discharging time, and t_c is the charging time (s) [9]. After 2000 GCD cycles at a current density of 2.5 A/g in the presence of $K_3Fe(CN)_6$ electrolyte, the WO_3/SnO_2 nanocomposite electrode demonstrated good cycling stability, capacitance retention of 94.7%, and a coulombic efficiency of 99.9%. The inset graph presents the GCD curves for the first 10 and the last 10 cycles, and the shapes of the curves remained triangular, which indicated the pseudocapacitive nature and good capacitive behavior even after 2000 cycles. For comparison, the WO_3 electrode exhibited lower capacitance retention (90.4%) under the same conditions. This difference indicated that $K_3Fe(CN)_6$ improved the stability of the electrode, not just the pseudocapacitor. EIS analyses of the WO_3, SnO_2, and WO_3/SnO_2 nanocomposite electrodes were carried out to determine the effects of K_3Fe $(CN)_6$ on the conductivities of these electrodes. In the electrolyte system containing 1 M Na_2SO_4 with 0.02 M $K_3Fe(CN)_6$, the R_{ct} values of the WO_3, SnO_2, and WO_3/SnO_2 nanocomposite electrodes were 1.71 Ω, 1.69 Ω, and 1.56 Ω, respectively, and the Rs values of these electrodes were 2.78 Ω, 2.13 Ω, and 1.65 Ω, respectively (Table 2).

Table 2. Charge Transfer Resistance (R_{ct}) and Electrochemical Resistance (R_s) of Different Electrodes with/without $K_3Fe(CN)_6$.

Electrode	With $K_3Fe(CN)_6$		Without $K_3Fe(CN)_6$	
	Rs (Ω)	Rct (Ω)	Rs (Ω)	Rct (Ω)
WO_3	2.78	1.71	2.37	2.12
SnO_2	2.13	1.69	2.32	1.94
WO_3/SnO_2	1.65	1.56	1.87	1.72

The WO_3/SnO_2 nanocomposite electrode exhibited a lower Rct than the other electrodes in the electrolyte systems with/without $K_3Fe(CN)_6$. For all electrodes used in this study, $K_3Fe(CN)_6$ drastically decreased R_{ct}, which indicated that $K_3Fe(CN)_6$ facilitated charge transfer between the active materials. That is, $K_3Fe(CN)_6$ activated the electrical behaviors of the metal oxides used in this study. The R_s values also showed improvement, except for that of the WO_3 electrode, which was attributed to an additional redox reaction occurring between the electrode surface and the electrolyte, in addition to the increased ion concentration of the electrolyte solution.

2.2.3. Electrochemical Performance of Symmetric Systems

For practical application of the WO_3/SnO_2 nanocomposite electrode, a symmetric supercapacitor system with identical electrodes was constructed with an aqueous electrolyte containing 1 M $NaSO_4$ and 0.02 M $K_3Fe(CN)_6$. The total mass of the WO_3/SnO_2 nanocomposite on both electrodes was ~3.4 mg (1.7 mg for each). To confirm the optimal voltage window of the device, CV curves were measured over different potential ranges (from 1.0 to 1.8 V) at a scan rate of 50 mVs^{-1}, as shown in (Figure 8a). The CV profile showed that the working potential was extended to 1.8 V, and water hydrolysis occurred at 1.9 V. As the potential range was increased, the shapes of the CV curves changed from quasi-rectangular (up to 1.4 V) to rectangular with redox peaks (higher than 1.6 V). This change indicated that a potential range larger than 1.6 V converted the pseudocapacitive mechanism to an energy storage mechanism, including the redox reactions of $[Fe(CN)_6]^{3-}/[Fe(CN)_6]^{4-}$ ions.

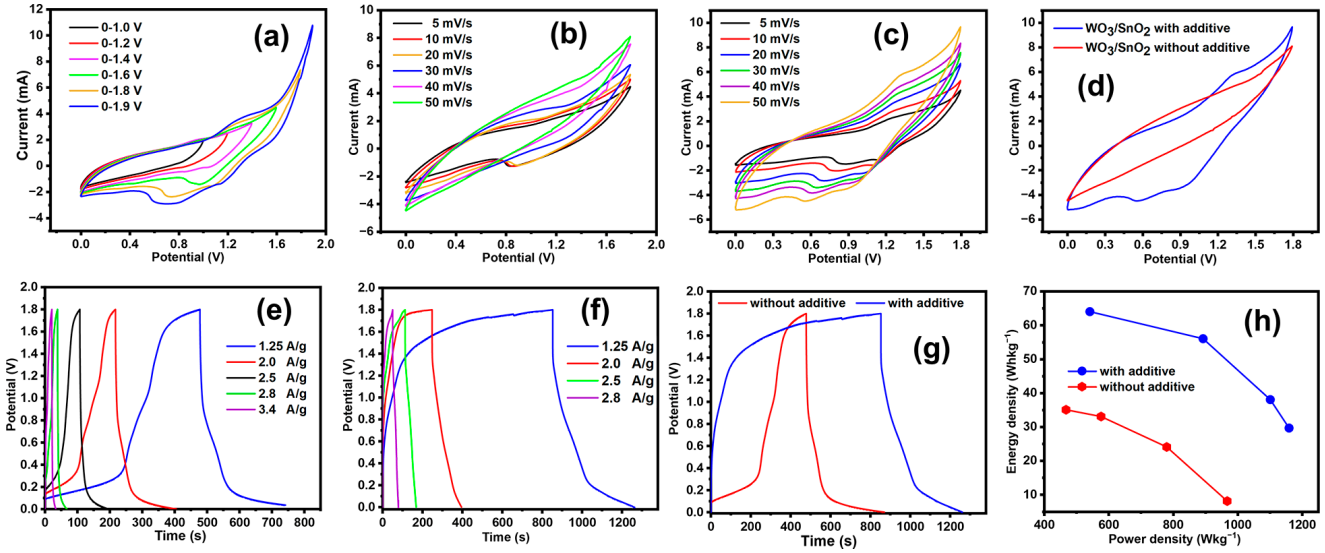


Figure 8. (**a**) CV curves of the WO_3/SnO_2 symmetric electrode with different applied potential windows at 50 mV/s, symmetric CV curves of the WO_3/SnO_2 symmetric electrode at different scan rates (**b**) without the redox-active electrolyte and (**c**) with the redox-active electrolyte; (**d**) comparison of the CV curves for the WO_3/SnO_2 symmetric device with and without the redox-active electrolyte at 50 mV/s; GCD curve for the WO_3/SnO_2 symmetric electrode at different current densities (**e**) without the redox-active electrolyte and (**f**) with the redox-active electrolyte; (**g**) comparison of the GCD curve-based symmetric electrode at 1.25 A/g; (**h**) Ragone plots of the WO_3/SnO_2 symmetric device.

The CV curves of the symmetric WO_3/SnO_2 nanocomposite electrode systems with and without $K_3Fe(CN)_6$ showed nearly rectangular shapes, which indicated pseudocapacitive behavior, even at a high scan rate of 50 mV/s (Figure 8b,c). Comparing the two systems, the CV profile of the WO_3/SnO_2 nanocomposite electrode with $K_3Fe(CN)_6$ had a greater area than that without $K_3Fe(CN)_6$, as expected from the half-cell experiment above (Figure 7b). GCD measurements of the symmetric WO_3/SnO_2 nanocomposite electrodes with and without K_3Fe $(CN)_6$ were also performed with various current densities (Figure 8e,f), and the GCD curves generated at 1.25 A/g were compared (Figure 8g). The IR drop in the initial phase of discharge was decreased in the presence of $K_3Fe(CN)_6$ (dropped from 1.8 V to ~1.0 V without $K_3Fe(CN)_6$ and from 1.8 V to ~1.3 V with $K_3Fe(CN)_6$). The specific capacitance values were determined at a current density of 1.25 A/g and were 285 F/g with $K_3Fe(CN)_6$ and 186 F/g without $K_3Fe(CN)_6$. The coulombic efficiencies were low in these cases, which could be explained by a minor water hydrolysis and the diffusion of $[Fe(CN)_6]^{3-}$/$[Fe$ $(CN)_6]^{4-}$ ions. At higher potential than 1.6 V, the edge of water electrolysis started (Figure 8a), and the minor gas generation resulted in the energy loss. Using $K_3Fe(CN)_6$, the reaction products ($[Fe(CN)_6]^{3-}$ and $[Fe(CN)_6]^{4-}$, mutually) diffused into the whole electrolyte solution in the cell, which decreased the availability of these ions for the discharge process [28].

The specific energy density (SE) and the specific power density (SP) of the WO_3/SnO_2 symmetric supercapacitor system with/without redox activity were important parameters for determining the feasibility of the device application. S_E and S_P were calculated using Equations (12) and (13) [53,54]:

$$S_E(\text{Whkg}^{-1}) = \frac{I}{M(3600)} \int_0^{t_d} V dt \quad (12)$$

$$S_p(\text{W Kg}^{-1}) = \frac{ED\ X\ 3600}{t_d} \quad (13)$$

where M is the total mass of both the positive and negative electrodes, I is the current, and V is the potential as a function of discharge time (t_d). The Ragone diagram for the energy density vs. power density of the WO_3/SnO_2 nanocomposite electrodes with/without additive is shown in (Figure 8h). The WO_3/SnO_2 symmetric supercapacitor system with the $K_3Fe(CN)_6$ electrolyte exhibited the highest S_E of 64 $Whkg^{-1}$ at a S_P of 542 Wkg^{-1}, whereas without $K_3Fe(CN)_6$, the S_E was 35 $Whkg^{-1}$ for a S_P of 468 Wkg^{-1} (in both cases, the current density was 1.25 A/g). Compared with previous reports, the symmetric device with the WO_3/SnO_2 nanocomposite electrodes exhibited excellent electrochemical performance in the $Na_2SO_4/K_3Fe(CN)_6$ electrolyte (Table 3). In the symmetric system, the active materials simultaneously worked as positive (anode) and negative (cathode) electrodes, and the GCD curves confirmed the reversible balanced redox reactions occurring at the anode and cathode [61,62]. Although the WO_3/SnO_2 ratio and the concentration of $K_3Fe(CN)_6$ should be optimized in future studies, the approach in this study would be useful for designing metal oxide nanocomposites for supercapacitors.

Table 3. Comparison of the electrochemical performance for WO_3-based active electrode materials with the parameters for supercapacitor applications.

Electrode	Specific Capacitance (Fg^{-1})	Current Density (Ag^{-1})	Energy Density ($Whkg^{-1}$)	Power Density (Wkg^{-1})	Stability (Retention, Cycles)	Electrolyte	Ref.
MnO_2-WO_3	657@5 mVs^{-1}	NA	10.8	650	92%, 2000	Na_2SO_4	[21]
RuO_2-WO_3	NA	NA	16.92	540	NA	NA	[12]
WO_3-MnO_2/WO_3	88.6	4 $mAcm^{-2}$	24.13	915	95%, 2500	CMC-Na_2SO_4	[14]
WO_3-RGO	495	1	NA	NA	85%, 1000	0.5 M H_2SO_4	[13]
WO_3@CuO	248.2	1	NA	NA	85.2%, 1500	6 M KOH	[60]
WO_3/Se(ASC)	0.858	0.2	0.047	0.345	74%, 4000	PVA-H_2SO_4	[2]
WO_3/SnO_2	530@5 mVs^{-1}	NA	35	468	NA	1 M Na_2SO_4	This work
WO_3/SnO_2	640@5 mVs^{-1}	NA	64	542	94.7%, 2000	0.02 M $K_3Fe(CN)_6$/ 1 M Na_2SO_4	This work

3. Discussion

In this study, microspheres of WO_3, nanorods of SnO_2, and WO_3/SnO_2 nanocomposite thin films were synthesized via chemical bath deposition, electrodeposition, and calcination. The hexagonal phase of WO_3 and the tetragonal phase of SnO_2 were observed in both the single-component and nanocomposite materials. The average WO_3 crystal size in the nanocomposite was smaller than that in single-component WO_3. An interaction between WO_3 and the SnO_2 in the nanocomposite was also suggested by the shifts in binding energies measured by XPS. SEM observations indicated the mesoporous surface structures of these nanomaterials, which are preferable for supercapacitor applications.

The CV measurements revealed that the specific capacitance of the WO_3/SnO_2 nanocomposite electrode reached 530 Fg^{-1} without $K_3Fe(CN)_6$ and 640 Fg^{-1} with $K_3Fe(CN)_6$ at a low scan rate of 5 mV/s. The improved capacitance in the presence of $K_3Fe(CN)_6$ was explained by the redox reactions of $[Fe(CN)_6]^{3-}/[Fe(CN)_6]^{4-}$ ions, in addition to the redox reactions of the WO_3/SnO_2 nanocomposite. Moreover, the WO_3/SnO_2 nanocomposite and $K_3Fe(CN)_6$ could mutually facilitate their redox reactions. The improved specific capacitance was also observed for single-component electrodes (both of WO_3 and SnO_2). Therefore, this approach can be used for other electrodes using these metal oxides, although the reaction efficiency could be differed by the electrode species.

Using the symmetric configurations of WO_3/SnO_2 nanocomposite electrodes, the addition of $K_3Fe(CN)_6$ to the 1 M Na_2SO_4 electrolyte generated a high energy density and a power density of 64 $Whkg^{-1}$ at 542 Wkg^{-1}, respectively. The capacitive retention efficiencies for the WO_3/SnO_2 and WO_3 electrodes with the $K_3Fe(CN)_6$ electrolyte was 94.7% and

90.4%, respectively, as indicated by GCD curves after 2000 cycles at 2.5 Ag^{-1}. The higher cycling stability and the excellent coulombic efficiency (99.9%) of the WO_3/SnO_2 nanocomposite electrode relative to those of the pure WO_3 electrode were due to the high catalytic activity of the WO_3/SnO_2 nanocomposite for the redox reactions of $[Fe(CN)_6]^{3-}/[Fe(CN)_6]^{4-}$ ions. As a result, the binder-free WO_3/SnO_2 nanocomposite with a redox-active electrolyte constituted a promising system for pseudocapacitive energy storage devices. Although the optimal configuration of the WO_3/SnO_2 nanocomposite and the electrolyte system should be studied further in the future, this approach can also be used with other metal oxide nanocomposites in reactive electrolytes.

4. Materials and Methods

Sodium tungstate dihydrate ($Na_2WO_4 \cdot 2H_2O$) was purchased from Alfa Aesar India, and tin (II) chloride hydrate ($SnCl_2 \cdot 2H_2O$) was purchased from Alfa Aesar United States. Hydrochloric acid (HCl, ~35% *v/v*) and ammonium sulfate ($(NH_4)_2SO_4$) were purchased from Duksan. Carbon cloth (WOS1009) was obtained from CeTech Co., Ltd., and sodium sulfate (Na_2SO_4, anhydrous, $\geq$99%) was from Honeywell/Fluka. Potassium ferricyanide ($K_3Fe(CN)_6$, 99%) was purchased from Acros Organics. All of these chemicals were used without further purification. Aqueous solutions were freshly prepared with ultrapure water (resistivity of 18.2 MΩcm; Yamato, Japan) throughout the experiments. Characterization was performed over the range $2\theta = 10^\circ$ to 60° at room temperature with an X-ray diffractometer (XRD, Bruker, D2 phaser Karlsruhe, German) using a copper radiation source ($\lambda = 0.154$ nm), operating at 40 kV and 30 mA, with a step size of 0.05 and step time of 5 sec.; X-ray photoelectron spectroscopy (XPS, VG scientific ESCALAB 250, Birmingham, UK); and field emission scanning electron microscopy (FE-SEM, at 15 kV acceleration voltage) equipped with an energy-dispersive X-ray spectroscopy (EDS) analyzer (JSM-6500F, JEOL, Tokyo, Japan).

4.1. Chemical Bath Deposition of WO_3 Nanosphere Thin Films

WO_3 nanospheres were deposited on a carbon cloth substrate by the CBD method. First, a carbon cloth substrate (1×1 cm^2) was treated with 1 M HNO_3, acetone, ethanol, and water sequentially with ultrasonication for 20 min and then dried overnight in a vacuum. In a typical preparation of WO_3 nanospheres, $Na_2WO_4 \cdot H_2O$ (0.82 g) was dissolved in 50 mL of water. After stirring for 20 min, 1 M HCl was added dropwise to produce a pH of 1.2 ± 1.0. After stirring for 30 min, $(NH_4)_2SO_4$ (1.32 g) was added to the above solution. After stirring for 10 min, 40 mL of the above mixture was transferred to a 100 mL beaker, and the carbon cloth substrate was immersed in it. Then, the beaker was heated on a hotplate at 80 °C for 4 h. The carbon cloth was removed from the bath, rinsed several times with water, and dried overnight at room temperature. Finally, the film was calcined at 400 °C for 2 h. The mass of WO_3 loaded onto the carbon cloth substrate was measured by subtracting the weight of the original carbon cloth substrate from the weight of the product and determined to be 1.2 mg.

4.2. Electrochemical Deposition of SnO_2 Nanorods

SnO_2 nanorods were synthesized through electrochemical deposition. First, a carbon cloth substrate with an area of 1×1 cm^2 was treated with 1 M HNO_3, acetone, ethanol, and water through ultrasonication and sequentially dried overnight at ambient temperature. Next, an aqueous solution of $SnCl_2$ (0.112 g) was prepared in 50 mL of water, and 2.6 mL of HCl was added. After stirring for 30 min, 25 mL of the solution was transferred to a 100 mL beaker, and a three-electrode system was set up: carbon cloth was used as the working electrode (WE), Ag/AgCl in 3 M Cl was used as the reference electrode (RE), and a platinum wire was used as the counter electrode (CE). Then, in a solution of $SnCl_2$ with HCl, potentiostatic electrodeposition was performed at an applied potential of -0.9 V for 10 min using a galvanostat/potentiostat (Hokuto-Denko, Model HA-151B) at ambient temperature. After deposition, the WE was rinsed with water and dried overnight at

ambient temperature. Finally, the deposited material on the carbon cloth was calcined at 400 °C for 2 h. The deposited mass was measured by subtracting the weight of the original carbon cloth substrate from the weight of the product and determined to be 0.4 mg.

4.3. Synthesis of a WO_3/SnO_2 Nanocomposite Electrode

WO_3/SnO_2 nanocomposite thin films were synthesized through CBD and the electrochemical deposition method. First, the carbon cloth substrate of area (1×1 cm^2) was sequentially treated by ultrasonication in 1 M HNO_3, acetone, ethanol, and ultrapure water and then dried overnight at ambient temperature. WO_3 microspheres were deposited on the carbon cloth by CBD, and then the carbon cloth/WO_3 was immersed in the $SnCl_2$/HCl solution (25 mL, 0.112 g, and 0.65 M) in a 100 mL beaker [63]. Then, the three-electrode system was set up: the WE were carbon cloth supported by WO_3 nanospheres, the RE was Ag/AgCl in 3 M Cl, and the CE was a platinum wire. Then, potentiostatic electrodeposition was performed at an applied potential of −0.9 V for 10 min using a galvanostat/potentiostat (Hokuto-Denko, Model HA-151B) at ambient temperature. After deposition, the WE were rinsed with water and then dried overnight at ambient temperature. Finally, the deposited material on the carbon cloth was calcined at 400 °C for 2 h on a hot plate. The deposited mass was measured by subtracting the weight of the original carbon cloth substrate from the weight of the product and was determined to be 1.6 mg.

4.4. Electrochemical Analyses

All electrochemical analyses were performed using a standard three-electrode system in an electrochemical cell connected to an electrochemical workstation (ZAHNER mass system, model xpot-26366, Germany). An Ag/AgCl electrode in 3 M KCl was used as the RE; a Pt wire as CE; and the WO_3, SnO_2, and WO_3/SnO_2 nanocomposites formed on carbon cloth were used as WEs. An aqueous solution of 1 M Na_2SO_4 with/without 0.02 M $K_3Fe(CN)_6$ was used as the electrolyte for all electrochemical measurements. The electrochemical performance of WO_3 and SnO_2, as well as the WO_3/SnO_2 nanocomposite electrodes, was studied using cyclic voltammetry (CV) over the range −0.2 V to 0.7 V vs. Ag/AgCl at different scan rates and galvanostatic charge-discharge (GCD) at different current densities. Electrochemical impendence spectroscopy (EIS) was performed with an amplitude of 10 mV over the frequency range 100 kHz to 100 mHz in an open circuit and described with a Nyquist plot.

5. Conclusions

In this work, we developed a preparation method of WO_3/SnO_2 nanocomposite on carbon cloth for supercapacitor electrodes. WO_3 nanospheres were first deposited on a carbon cloth substrate by a chemical bath deposition method, and then a SnO_2 layer was formed by an electrochemical deposition and calcination. The WO_3/SnO_2 nanocomposite on carbon cloth exhibited a higher specific capacitance (530 F/g at 5 mV/s scan rate) than that of single-component electrodes (240 F/g for WO_3 and 140 F/g for SnO_2) in an aqueous electrolyte of 1M Na_2SO_4. The addition of 0.02 M $K_3Fe(CN)_6$ redox-active electrolyte into the 1M Na_2SO_4 electrolyte further improved the charge storage performance of electrodes (440 F/g for WO_3, 310 F/g for SnO_2, and 640 F/g for WO_3/SnO_2 nanocomposite). These results show the synergistic effects of WO_3/SnO_2 nanocomposites and the advantages of using redox-active electrolytes for supercapacitor systems. Using a symmetric configuration of WO_3/SnO_2 nanocomposite electrodes, the electrolyte solution of 0.02 M$K_3Fe(CN)_6$ and 1 M Na_2SO_4 electrolyte demonstrated a high energy density and a power density of 64 Whkg^{-1} at 542 Wkg^{-1}, respectively. The capacitive retention efficiency for the WO_3/SnO_2 and WO_3 electrodes with the $K_3Fe(CN)_6$ electrolyte was 94.7% after 2000 cycles at 2.5 Ag^{-1}. Thus, the WO_3/SnO_2 nanocomposite electrode grown on carbon cloth is a promising candidates as a binder-free electrode for the high performance of a supercapacitor device, and the supercapacitor system using redox-active $K_3Fe(CN)_6$

electrolyte was proposed. These strategies developed in this study can also be applied to other metal oxide nanocomposites to improve the performance of supercapacitors.

Supplementary Materials: The following supporting information can be downloaded at: https://www.mdpi.com/article/10.3390/ijms24076045/s1.

Author Contributions: Conceptualization, T.D.M. and M.U.; methodology, M.U.; software, M.U.; formal analysis, T.D.M.; investigation, T.D.M.; resources, M.U.; data curation, T.D.M.; writing—original draft preparation, T.D.M.; writing—review and editing, M.U.; visualization, T.D.M.; supervision, M.U.; project administration, M.U.; funding acquisition, M.U. All authors have read and agreed to the published version of the manuscript.

Funding: This research was funded by the Ministry of Science and Technology of the Republic of China, [MOST 109-2221-E-011-062-].

Institutional Review Board Statement: Not applicable.

Informed Consent Statement: Not applicable.

Data Availability Statement: The data presented in this study are available on request from the corresponding author.

Acknowledgments: This investigation was partly supported by the Graduate Institute of Applied Science and Technology, National Taiwan University of Science and Technology.

Conflicts of Interest: The authors declare no conflict of interest.

References

1. Shinde, P.A.; Lokhande, A.C.; Patil, A.M.; Lokhande, C.D. Facile synthesis of self-assembled WO_3 nanorods for high-performance electrochemical capacitor. *J. Alloys Compd.* **2019**, *770*, 1130–1137. [CrossRef]
2. Barik, R.; Yadav, A.K.; Jha, S.N.; Bhattacharyya, D.; Ingole, P.P. Two-dimensional tungsten oxide/selenium nanocomposite fabricated for flexible supercapacitors with higher operational voltage and their charge storage mechanism. *ACS Appl. Mater. Interfaces* **2021**, *13*, 8102–8119. [CrossRef] [PubMed]
3. Debelo, T.T.; Ujihara, M. Effect of simultaneous electrochemical deposition of manganese hydroxide and polypyrrole on structure and capacitive behavior. *J. Electroanal. Chem.* **2020**, *859*, 113825. [CrossRef]
4. Mevada, C.; Mukhopadhyay, M. High mass loading tin oxide-ruthenium oxide-based nanocomposite electrode for supercapacitor application. *J. Energy Storage* **2020**, *31*, 101587. [CrossRef]
5. Kariper, İ.; Tezel, F.M.; Gökkuş, Ö. Synthesize of WO_3 thin film supercapacitor and its characterization. *Phys. Lett. A* **2021**, *388*, 127059. [CrossRef]
6. Abebe, E.M.; Ujihara, M. Influence of Temperature on ZnO/Co_3O_4 Nanocomposites for High Energy Storage Supercapacitors. *ACS Omega* **2021**, *6*, 23750. [CrossRef]
7. Abebe, E.M.; Ujihara, M. Simultaneous Electrodeposition of Ternary Metal Oxide Nanocomposites for High-Efficiency Supercapacitor Applications. *ACS Omega* **2022**, *7*, 17161–17174. [CrossRef] [PubMed]
8. Kang, Y.; Li, Z.; Xu, K.; He, X.; Wei, S.; Cao, Y. Hollow SnO_2 nanospheres with single-shelled structure and the application for supercapacitors. *J. Alloys Compd.* **2019**, *779*, 728–734. [CrossRef]
9. Debelo, T.T.; Ujihara, M. Electrodeposition of binder-free polypyrrole on a three-dimensional flower-like nanosheet of manganese oxides containing pyrrole derivative for supercapacitor electrode. *J. Mater. Chem. A* **2022**, *278*, 125690. [CrossRef]
10. Poudel, M.B.; Lohani, P.C.; Kim, A.A. Synthesis of silver nanoparticles decorated tungsten oxide nanorods as high-performance supercapacitor electrode. *Chem. Phys. Lett.* **2022**, *804*, 139884. [CrossRef]
11. Nithya, V.; Arul, N.S. Review on α-Fe_2O_3 based negative electrode for high performance supercapacitors. *J. Power Sources* **2016**, *327*, 297–318. [CrossRef]
12. Shinde, P.A.; Lokhande, A.C.; Chodankar, N.R.; Patil, A.M.; Kim, J.H.; Lokhande, C.D. Temperature dependent surface morphological modifications of hexagonal WO_3 thin films for high performance supercapacitor application. *Electrochim. Acta* **2017**, *224*, 397–404. [CrossRef]
13. Ji, S.-H.; Chodankar, N.R.; Kim, D.-H. Aqueous asymmetric supercapacitor based on RuO_2-WO_3 electrodes. *Electrochim. Acta* **2019**, *325*, 134879. [CrossRef]
14. Chu, J.; Lu, D.; Wang, X.; Wang, X.; Xiong, S. WO_3 nanoflower coated with graphene nanosheet: Synergetic energy storage composite electrode for supercapacitor application. *J. Alloys Compd.* **2017**, *702*, 568–572. [CrossRef]
15. Shinde, P.A.; Lokhande, V.C.; Patil, A.M.; Ji, T.; Lokhande, C.D. Single-step hydrothermal synthesis of WO_3-MnO_2 composite as an active material for all-solid-state flexible asymmetric supercapacitor. *Int. J. Hydrogen Energy* **2018**, *43*, 2869–2880. [CrossRef]
16. Kumar, R.D.; Andou, Y.; Karuppuchamy, S. Synthesis and characterization of nanostructured Ni-WO_3 and $NiWO_4$ for supercapacitor applications. *J. Alloys Compd.* **2016**, *654*, 349–356. [CrossRef]

17. Kumar, R.D.; Karuppuchamy, S. Microwave mediated synthesis of nanostructured Co-WO_3 and $CoWO_4$ for supercapacitor applications. *J. Alloys Compd.* **2016**, *674*, 384–391. [CrossRef]
18. Hai, Z.; Akbari, M.K.; Xue, C.; Xu, H.; Solano, E.; Detavernier, C.; Hu, J.; Zhuiykov, S. Atomically-thin WO_3/TiO_2 heterojunction for supercapacitor electrodes developed by atomic layer deposition. *Compos. Commun.* **2017**, *5*, 31–35. [CrossRef]
19. Periasamy, P.; Krishnakumar, T.; Sandhiya, M.; Sathish, M.; Chavali, M.; Siril, P.F.; Devarajan, V. Preparation and comparison of hybridized WO_3–V_2O_5 nanocomposites electrochemical supercapacitor performance in KOH and H_2SO_4 electrolyte. *Mater. Lett.* **2019**, *236*, 702–705. [CrossRef]
20. Xu, Y.; Wang, L.; Zhou, Y.; Guo, J.; Zhang, S.; Lu, Y. Synthesis of heterostructure SnO_2/graphitic carbon nitride composite for high-performance electrochemical supercapacitor. *J. Electroanal. Chem.* **2019**, *852*, 113507. [CrossRef]
21. Shinde, P.A.; Lokhande, V.C.; Ji, T.; Lokhande, C.D. Facile synthesis of hierarchical mesoporous weirds-like morphological MnO_2 thin films on carbon cloth for high performance supercapacitor application. *J. Colloid Interface Sci.* **2017**, *498*, 202–209. [CrossRef] [PubMed]
22. Shinde, P.A.; Lokhande, V.C.; Patil, A.M.; Ji, T.; Lokhande, C.D. Design and synthesis of hierarchical mesoporous WO_3-MnO_2 composite nanostructures on carbon cloth for high-performance supercapacitors. *J. Electrochem. Sci. Technol.* **2017**, *3*, 35–48. [CrossRef]
23. Veerasubramani, G.K.; Krishnamoorthy, K.; Kim, S.J. Improved electrochemical performances of binder-free CoMoO4 nanoplate arrays@ Ni foam electrode using redox additive electrolyte. *J. Power Sources* **2016**, *306*, 378–386. [CrossRef]
24. Ojha, G.P.; Pant, B.; Acharya, J.; Park, M. Prussian red anions immobilized freestanding three-dimensional porous carbonaceous networks: A new avenue to attain capacitor-and faradic-type electrodes in a single frame for 2.0 V hybrid supercapacitors. *ACS Sustain. Chem. Eng.* **2022**, *10*, 2994–3006. [CrossRef]
25. Sankar, K.V.; Selvan, R.K. Improved electrochemical performances of reduced graphen oxide based supercapacitor using redox additive electrolyte. *Carbon* **2015**, *90*, 260–273. [CrossRef]
26. Huang, X.; Wang, Q.; Chen, X.Y.; Zhang, Z.J. The effects of amine/nitro/hydroxyl groups on the benzene rings of redox additives on the electrochemical performance of carbon-based supercapacitors. *Phys. Chem. Chem. Phys.* **2016**, *18*, 10438–10452. [CrossRef]
27. Han, X.; Jiang, T.; Chen, X.; Jiang, D.; Xie, K.; Jiang, Y.; Wang, Y. Electrolyte additive induced fast-charge/slow-discharge process: Potassium ferricyanide and potassium persulfate for CoO-based supercapacitors. *J. Colloid Interface Sci.* **2020**, *576*, 505–513. [CrossRef]
28. Lee, J.; Choudhury, S.; Weingarth, D.; Kim, D.; Presser, V. High performance hybrid energy storage with potassium ferricyanide redox electrolyte. *ACS Appl. Mater. Interfaces* **2016**, *8*, 23676–23687. [CrossRef]
29. Lokhande, V.; Lokhande, A.; Namkoong, G.; Kim, J.H.; Ji, T. Charge storage in WO_3 polymorphs and their application as supercapacitor electrode material. *Results Phys.* **2019**, *12*, 2012–2020. [CrossRef]
30. Zheng, F.; Song, S.; Lu, F.; Li, R.; Bu, N.; Liu, J.; Li, Y.; Hu, P.; Zhen, Q. Hydrothermal preparation, growth mechanism and supercapacitive properties of WO $_3$ nanorod arrays grown directly on a Cu substrate. *CrystEngComm* **2016**, *18*, 3891–3904. [CrossRef]
31. Gao, L.; Wang, X.; Xie, Z.; Song, W.; Wang, L.; Wu, X.; Qu, F.; Chen, D.; Shen, G. High-performance energy-storage devices based on WO_3 nanowire arrays/carbon cloth integrated electrodes. *J. Mater. Chem. A* **2013**, *1*, 7167–7173. [CrossRef]
32. Nayak, A.K.; Ghosh, R.; Santra, S.; Guha, P.K.; Pradhan, D. Hierarchical nanostructured WO $_3$–SnO $_2$ for selective sensing of volatile organic compounds. *Nanoscale* **2015**, *7*, 12460–12473. [CrossRef] [PubMed]
33. Zhu, Y.; Wang, H.; Liu, J.; Yin, M.; Yu, L.; Zhou, J.; Liu, Y.; Qiao, F. High-performance gas sensors based on the WO_3-SnO_2 nanosphere composites. *J. Alloys Compd.* **2019**, *782*, 789–795. [CrossRef]
34. Darwish, A.M.; Eisa, W.H.; Shabaka, A.A.; Talaat, M.H. Investigation of factors affecting the synthesis of nano-cadmium sulfide by pulsed laser ablation in liquid environment. *Spectrochim. Acta Part A Mol. Biomol. Spectrosc.* **2016**, *153*, 315–320. [CrossRef] [PubMed]
35. Hasanin, M.S.; Mostafa, A.M.; Mwafy, E.A.; Darwesh, O.M. Eco-friendly cellulose nano fibers via first reported Egyptian Humicola fuscoatra Egyptia X_4: Isolation and characterization. *Environ. Nanotechnol. Monit. Manag.* **2018**, *10*, 409–418. [CrossRef]
36. Geleta, T.A.; Imae, T. Influence of additives on zinc oxide-based dye sensitized solar cells. *Bull. Chem. Soc. Jpn.* **2020**, *93*, 611. [CrossRef]
37. Shao, H.; Huang, M.; Fu, H.; Wang, S.; Wang, L.; Lu, J.; Wang, Y.; Yu, K. Hollow WO_3/SnO_2 hetero-nanofibers: Controlled synthesis and high efficiency of acetone vapor detection. *Front. Chem.* **2019**, *7*, 785. [CrossRef] [PubMed]
38. Wu, C.-M.; Motora, K.G.; Chen, G.-Y.; Kuo, D.-H.; Gultom, N.S. Highly efficient MoS_2@Cs_xWO_3 nanocomposite hydrogen gas sensors. *Front. Mater.* **2022**, *9*, 18. [CrossRef]
39. Claros, M.; Setka, M.; Jimenez, Y.P.; Vallejos, S. AACVD synthesis and characterization of iron and copper oxides modified ZnO structured films. *J. Nanomater.* **2020**, *10*, 471. [CrossRef]
40. Motsoeneng, R.G.; Kortidis, I.; Ray, S.S.; Motaung, D.E. Designing SnO_2 nanostructure-based sensors with tailored selectivity toward propanol and ethanol vapors. *J. Alloys Compd.* **2019**, *4*, 13696–13709. [CrossRef]
41. Ciftyürek, E.; Šmíd, B.; Li, Z.; Matolín, V.; Schierbaum, K. Spectroscopic understanding of SnO_2 and WO_3 metal oxide surfaces with advanced synchrotron based; XPS-UPS and near ambient pressure (NAP) XPS surface sensitive techniques for gas sensor applications under operational conditions. *J. Sens.* **2019**, *19*, 4737. [CrossRef] [PubMed]

42. Farhadian, M.; Sangpour, P.; Hosseinzadeh, G. Morphology dependent photocatalytic activity of WO_3 nanostructures. *J. Energy Chem.* **2015**, *24*, 171–177. [CrossRef]
43. Han, C.; Zhang, B.; Zhao, K.; Meng, J.; He, Q.; He, P.; Yang, W.; Li, Q.; Mai, L. Oxalate-assisted formation of uniform carbon-confined SnO_2 nanotubes with enhanced lithium storage. *Chem. Commun.* **2017**, *53*, 9542–9545. [CrossRef] [PubMed]
44. Liu, M.; Xu, P.; Wang, G.; Yan, J. SnO_2 Nanorod arrays grown on carbon cloth as a flexible binder-free electrode for high-performance lithium batteries. *J. Electron. Mater.* **2019**, *48*, 8206–8211. [CrossRef]
45. Zhao, Y.-F.; Sun, Y.-P.; Yin, X.; Yin, G.-C.; Wang, X.-M.; Jia, F.-C.; Liu, B. Effect of surfactants on the microstructures of hierarchical SnO_2 blooming nanoflowers and their gas-sensing properties. *Nanoscale Res. Lett.* **2018**, *13*, 54. [CrossRef] [PubMed]
46. Gupta, S.P.; Nishad, H.H.; Chakane, S.D.; Gosavi, S.W.; Late, D.J.; Walke, P.S. Phase transformation in tungsten oxide nanoplates as a function of post-annealing temperature and its electrochemical influence on energy storage. *Nanoscale Adv.* **2020**, *2*, 4689–4701. [CrossRef]
47. Huang, H.; Tan, O.; Lee, Y.; Tse, M.; Guo, J.; White, T. In situ growth of SnO_2 nanorods by plasma treatment of SnO_2 thin films. *J. Nanotechnol.* **2006**, *17*, 3668. [CrossRef]
48. Li, K.-D.; Chen, P.-W.; Chang, K.-S.; Hsu, S.-C.; Jan, D.-J. Indium-Zinc-Tin-Oxide Film Prepared by Reactive Magnetron Sputtering for Electrochromic Applications. *Materials* **2018**, *11*, 2221. [CrossRef]
49. Yang, F.; Jia, J.; Mi, R.; Liu, X.; Fu, Z.; Wang, C.; Liu, X.; Tang, Y. Fabrication of $WO_3 \cdot 2H_2O$/BC hybrids by the radiation method for enhanced performance supercapacitors. *Front. Chem.* **2018**, *6*, 290. [CrossRef]
50. Wang, S.; Xu, H.; Hao, T.; Wang, P.; Zhang, X.; Zhang, H.; Xue, J.; Zhao, J.; Li, Y. In situ XRD and operando spectra-electrochemical investigation of tetragonal WO_3-x nanowire networks for electrochromic supercapacitors. *NPG Asia Mater.* **2021**, *13*, 51. [CrossRef]
51. Ashraf, M.; Shah, S.S.; Khan, I.; Aziz, M.A.; Ullah, N.; Khan, M.; Adil, S.F.; Liaqat, Z.; Usman, M.; Tremel, W. A High-Performance Asymmetric Supercapacitor Based on Tungsten Oxide Nanoplates and Highly Reduced Graphene Oxide Electrodes. *Chem. A Eur. J.* **2021**, *27*, 6973–6984. [CrossRef] [PubMed]
52. Angelin, M.D.; Rajkumar, S.; Merlin, J.P.; Xavier, A.R.; Franklin, M.; Ravichandran, A. Electrochemical investigation of Zr-doped ZnO nanostructured electrode material for high-performance supercapacitor. *Ionics* **2020**, *26*, 5757–5772. [CrossRef]
53. Mathis, T.S.; Kurra, N.; Wang, X.; Pinto, D.; Simon, P.; Gogotsi, Y. Energy storage data reporting in perspective—Guidelines for interpreting the performance of electrochemical energy storage systems. *Adv. Energy Mater.* **2019**, *9*, 1902007. [CrossRef]
54. Pham, D.T.; Baboo, J.P.; Song, J.; Kim, S.; Jo, J.; Mathew, V.; Alfaruqi, M.H.; Sambandam, B.; Kim, J. Facile synthesis of pyrite (FeS_2/C) nanoparticles as an electrode material for non-aqueous hybrid electrochemical capacitors. *Nanoscale* **2018**, *10*, 5938–5949. [CrossRef] [PubMed]
55. Nagaraju, P.; Alsalme, A.; Alkathiri, A.M.; Jayavel, R. Rapid synthesis of WO_3/graphene nanocomposite via in-situ microwave method with improved electrochemical properties. *J. Phys. Chem. Solids* **2018**, *120*, 250–260. [CrossRef]
56. Huang, Y.; Li, M.; Chen, S.; Sun, P.; Lv, X.; Li, B.; Fang, L.; Sun, X. Constructing aqueous Zn//Ni hybrid battery with NiSe nanorod array on nickel foam and redox electrolytes for high-performance electrochemical energy storage. *Appl. Surf. Sci.* **2021**, *562*, 150222. [CrossRef]
57. Chowdhury, A.; Biswas, S.; Singh, T.; Chandra, A. Redox mediator induced electrochemical reactions at the electrode-electrolyte interface: Making sodium-ion supercapacitors a competitive technology. *Electrochem. Sci. Adv.* **2022**, *2*, e2100030. [CrossRef]
58. Kim, H.-S.; Cook, J.B.; Lin, H.; Ko, J.S.; Tolbert, S.H.; Ozolins, V.; Dunn, B. Oxygen vacancies enhance pseudocapacitive charge storage properties of MoO_{3-x}. *Nat. Mater.* **2017**, *16*, 454–460. [CrossRef]
59. Dong, X.; Chen, L.; Liu, J.; Haller, S.; Wang, Y.; Xia, Y. Environmentally-friendly aqueous Li (or Na)-ion battery with fast electrode kinetics and super-long life. *Sci. Adv.* **2016**, *2*, e1501038. [CrossRef]
60. Teli, A.M.; Beknalkar, S.A.; Pawar, S.A.; Dubal, D.P.; Dongale, T.D.; Patil, D.S.; Patil, P.S.; Shin, J.C. Effect of concentration on the charge storage kinetics of nanostructured MnO_2 thin-film supercapacitors synthesized by the hydrothermal method. *Energies* **2020**, *13*, 6124. [CrossRef]
61. Sahoo, M.K.; Rao, G.R. A high energy flexible symmetric supercapacitor fabricated using N-doped activated carbon derived from palm flowers. *Nanoscale Adv.* **2021**, *3*, 5417–5429. [CrossRef] [PubMed]
62. Tian, J.; Lin, B.; Sun, Y.; Zhang, X.; Yang, H. Porous WO_3@CuO composites derived from polyoxometalates@ metal organic frameworks for supercapacitor. *Mater. Lett.* **2017**, *206*, 91–94. [CrossRef]
63. Gao, L.; Qu, F.; Wu, X. Hierarchical WO_3@SnO_2 core–shell nanowire arrays on carbon cloth: A new class of anode for high-performance lithium-ion batteries. *J. Mater. Chem. A* **2014**, *2*, 7367–7372. [CrossRef]

Disclaimer/Publisher's Note: The statements, opinions and data contained in all publications are solely those of the individual author(s) and contributor(s) and not of MDPI and/or the editor(s). MDPI and/or the editor(s) disclaim responsibility for any injury to people or property resulting from any ideas, methods, instructions or products referred to in the content.